Radiation Patterns and Virtual Shot Gathers in High-Speed Rail Seismic Wavefield: Mechanisms, Observations, and Monitoring Implications

高铁波场内的局域共振现象： 来自多尺度观测台阵的虚拟炮集与振幅规律的证据

Yon

[1]State Key Laboratory of Lithospheric and Environmental Coevolution, Institute of Geology and Geophysics, Chinese Academy of Sciences, Beijing 100029, China

[2]School of Earth and Space Sciences, Peking University, Beijing 100871, China

[3]Institute of Geophysics, China Earthquake Administration, Beijing 100081, China

[4]Hebei Earthquake Agency, Shijiazhuang 050021, China

Key points

- Virtual shot gathers of high-speed rail (HSR) exhibit radiation patterns due to the dual coherence from train geometry and bridge piers.
- The theoretical HSR radiation patterns predict azimuth- and frequency-dependent energy focusing, validated by over 5,400 train events.
- The HSR radiation pattern produces sharply contrasting effects for surface waves and a dispersive high-velocity seismic phase.

Abstract

High-speed rail (HSR) vibrations, characterized by high energy and strong repeatability, are a promising passive seismic source for near-surface monitoring. HSR sources not only produce discrete-spectrum wavelets excited by train wheel assemblies, but are also subject to spatial coherence modulated by equally spaced bridge piers, forming a unique, strongly coherent source. To fully exploit their monitoring potential, the coupling mechanism between HSR coherence and seismic interferometry must be clarified. We theoretically derive the radiation patterns of HSR sources, elucidating how source coherence impacts HSR seismic interferometry. Using field data from more than 5,400 train events in the Baoding region, we reconstruct virtual shot gathers (VSGs) along different azimuths for validation. The results in field data demonstrate that both surface waves and a seismic phase close to P-wave velocity, excited by HSR sources, exhibit significant azimuthal dependence in spectral energy. This dependence closely matches the theoretical predictions. These findings of HSR provide a theoretical basis for understanding phase generation, constraining phase energy, and designing targeted detection and monitoring methodologies.

Plain Language Summary

High-speed trains generate powerful and highly regular ground vibrations, acting like a "seismic radar". This regularity comes from two features: the repeating pattern of train wheels creates distinct frequency lines, and the evenly spaced bridge piers act like a directional antenna, focusing the seismic energy into specific directions. We analyzed vibrations from over 5,400 trains to create virtual seismic shots. We found that surface waves of HSR are strongest in front of the train, while a fast, deep-traveling wave is the main signal along the track. The way the energy of these waves changes with direction and frequency perfectly matches our theoretical predictions. Understanding this "radiation pattern" is the key to using the everyday rumble of trains to efficiently monitor changes underground, such as groundwater levels or the basement health of the railway foundation.

1 Introduction

Monitoring shallow subsurface dynamics is a pivotal frontier in seismology, crucial for revealing dynamic underground processes and providing key technical support

for subsurface space utilization (Shen et al., 2024; Mao et al., 2025; Meng & Liu, 2025). Among various techniques, passive seismic interferometry using traffic-induced sources has emerged as a vital and cost-effective approach. Such sources not only provide stable illumination for subsurface imaging along transport corridors (Brenguier et al., 2019; Sheng et al., 2022; Mukherjee et al., 2026), but also enable direct monitoring of the state of media beneath infrastructure (Cheng et al., 2025; Cunha Teixeira et al., 2025).

For conventional traffic sources, speed and spatial distribution of vehicles are stochastic, so that the wavefield can be approximated as incoherent noise. Stable virtual phase signals can be extracted through conventional seismic interferometry (Nakata et al., 2011, 2015; Behm & Snieder, 2013; Quiros et al., 2016; Mi et al., 2022). Monitoring based on retrieved ballistic waves has the potential to provide more precise localization of depth-dependent changes compared to coda-wave methods (Brenguier et al., 2020; Mordret et al., 2020; Shen et al., 2024). Yet, not all traffic sources are purely stochastic and some exhibit intrinsic regularity. Studying and exploiting the source regularity can help improve monitoring temporal resolution while distinguishing source variations from true subsurface changes.

High-speed rail (HSR) is a typical traffic source that provides strong, well-characterised regularity. The regularity of HSR first stems from source wavelet coherence. A train consists of numerous repeating carriages and wheel assemblies, imparting a distinctive discrete spectrum to the excited seismic wavelets (Chen et al., 2004; L. Li et al., 2004; Lavoué et al., 2021). The high technical uniformity of HSR rolling stock further reinforces this discrete spectrum, enabling a unified source wavelet governed by train speed and fixed wheel assembly spacing (Jiang et al., 2019; X. Wang et al., 2019; Liu et al., 2021b). This grants HSR sources quasi-active-source properties, prompting studies to overcome wavelet coherence for imaging and inversion (G. Hu et al., 2019; Y. Shi et al., 2022; H. Wang & Chen, 2025; L. Wang et al., 2025). This frequency concentration enhances the signal-to-noise ratio and the potential for precise velocity-change monitoring.

Furthermore, HSR source regularity is compounded by spatial coherence induced by equally spaced bridge piers. HSR predominantly operates on viaducts with simply-supported spans, converting piers as actual points of seismic sources (Hung & Yang, 2001; Yang et al., 2003). Due to structural repetitiveness, seismic waves excited at different piers are highly coherent when a train passes at constant speed, generating significant

spatial interference effects (Wen et al., 2019). This interference induces an apparent HSR Doppler effect (Wen et al., 2021; Jiang et al., 2022; Y. Shi et al., 2022), selectively radiating energy toward specific azimuths, forming a "seismic radar"-like radiation pattern that focuses energy in specific directions.

However, the dual coherence formed by wavelet discrete spectrum and pier spatial interference significantly increases the complexity of the HSR wavefield. Currently, extracting effective signals from this complex wavefield primarily relies on seismic interferometry to construct virtual shot gathers (VSGs) (Zhang et al., 2019; Liu et al., 2021a; Yin et al., 2024). Common processing strategies, such as deconvolution or spectral whitening combined with event stacking, aim to suppress coherence to extract empirical Green's functions (Mi et al., 2023; Hong et al., 2024; Chang et al., 2025). However, a core question remains: How does the inherent dual coherence of HSR sources fundamentally shape the phase signals within VSGs? Existing studies, often limited in observational scale, have yet to provide a systematic theoretical framework that links train speed, frequency band, azimuth, and external noise to the final interferometric result. Answering this is critical to fully harness properties of HSR seismic signals and leverage their regularity for targeted detection and monitoring applications.

Therefore, this study investigates both theoretical and observational aspects. Theoretically, we analyze HSR source coherence and its impact on seismic interferometry, formalize the concept of HSR source radiation patterns, and validate it via simulation. Observationally, based on seismic data from over 5,400 train events of Beijing-Guangzhou HSR in the Baoding region, we obtain multiple VSGs, focusing on analyzing surface waves and a dispersive seismic phase close to P-wave velocity generated by HSR. By examining their systematic variations in frequency and azimuth, we validate the theoretical results and elucidate their specific radiation pattern characteristics. Finally, we discuss the formation mechanisms of different HSR phases and outline future directions for monitoring applications.

2 Theory: Seismic Interferometry and Radiation Patterns of HSR Sources

2.1 Dual Coherence of HSR Sources

The unique regularity of HSR sources stems from dual coherence: temporal wavelet coherence and spatial pier-array coherence. This concept is key to understanding the dis-

tinctiveness of HSR seismic interferometry results, manifesting as wavefield frequency components characterized by train frequencies and pier frequencies.

First, the HSR source can be modeled as a series of pier point sources modulated by a moving train (Fig. 1), with span L (typical 32 m). The train's periodic structure, such as carriage length L_c (typical 25 m), causes the excited pier wavelet $S(\omega, v)$ to exhibit a discrete spectrum with **train frequencies**:

$$f_c^m = m\frac{v}{L_c}, \quad m \in \mathbb{Z}^+, \tag{1}$$

as the dominant spectral lines (Yang et al., 1997, 2003; Liu et al., 2021b). The train frequency f_c^m varies with train speed v and carriage length L_c. For 300 km/h-class trains, the fundamental train frequency f_c^1 is approximately 3.3 Hz and its harmonics.

Second, when the train passes at constant speed v, neglecting incoherent factors like pier differences, different piers excite identical wavelets with fixed time delays, forming a linearly arranged coherent source array. Under a far-field approximation, the wavefield $d(\mathbf{r}, \omega)$ recorded at a receiver $\mathbf{r}$ at azimuth θ (relative to the train's direction) can be expressed as (Y. Shi et al., 2022):

$$\begin{aligned} d(\mathbf{r}, \omega) &= \sum_n S(\omega, v) G(\mathbf{r}|\mathbf{x}_s^n, \omega) \mathrm{e}^{\mathrm{i}\omega \frac{nL}{v}} \\ &= S(\omega, v) G(\mathbf{r}|\mathbf{x}_s^0, \omega) A\mathrm{e}^{\mathrm{i}\phi}, \end{aligned} \tag{2}$$

where n is the pier index, and $G(\mathbf{r}|\mathbf{x}_s^n, \omega)$ is the Green's function between the receiver and the n-th pier source. The summation term $A\mathrm{e}^{\mathrm{i}\phi}$ represents the difference between the HSR source wavefield and a point source wavefield, characterizing the spatial interference effect of the pier array. Constructive interference occurs when the time difference between adjacent pier signals, $\tau_I = L/v - (L\cos\theta)/c$ (c is the medium wave velocity), equals an integer multiple of the signal period. The corresponding characteristic frequencies:

$$f_I^n = \frac{n}{\tau_I} \quad (n \in \mathbb{Z}^+), \tag{3}$$

are termed **pier frequencies**, whose values vary with θ and c, embodying the Doppler shift effect of HSR (Jiang et al., 2022). For 32-m piers and 80 m/s (300 km/h-class) trains,

pier frequencies (f_I^n) shift around approximately 2.5 Hz and its harmonics across different azimuths, showing redshift ($\theta = \pi$) and blueshift ($\theta = 0$).

Therefore, the seismic wavefield generated by HSR is not solely controlled by the moving train source; it also incorporates periodic railway structural effects, forming a composite source structure. Specifically, the train frequencies (f_c^m) govern the composition of vibrations from different carriages into a time-domain wavelet at a single pier, while the pier frequencies (f_I^n) control the spatial combination of vibrations from different piers into the observed wavefield. Together, these two sets of frequencies determine the overall morphology of the HSR wavefield.

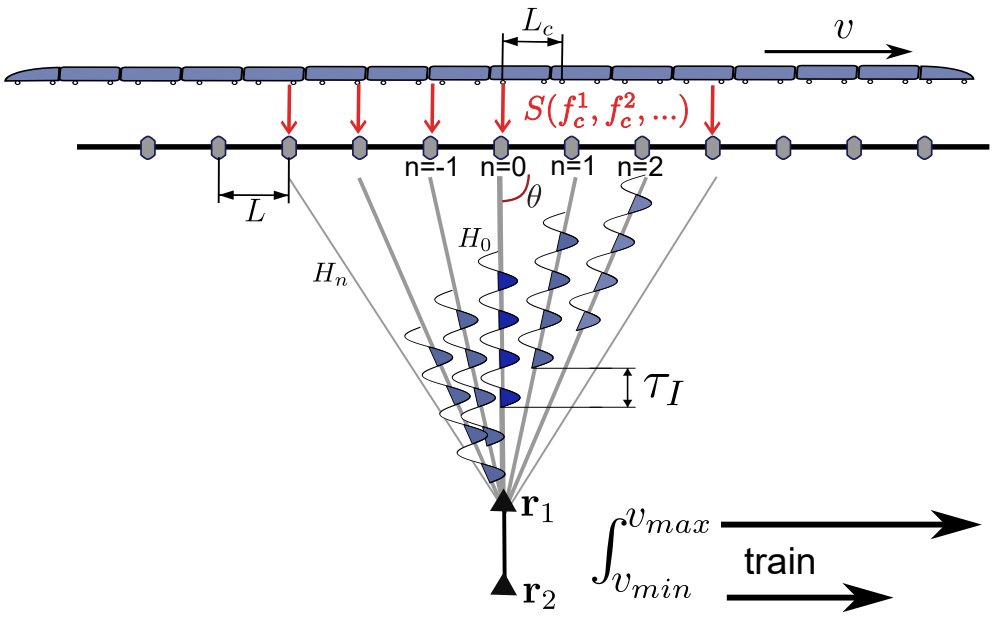


Figure 1. Schematic of HSR wavefield. The train uses a 16-carriage model with carriage spacing $L_c \approx 25$ m. Under train speed v, it generates wavelet S excitation at individual piers, with characteristic frequencies being f_c. The bridge consists of equally spaced piers with $L \approx 32$ m, and piers excite identical wavelets with fixed time delays. Under the combined effect of excitation time delay and path difference, the arrival time difference between adjacent pier waves is τ_I, with characteristic frequencies being f_I. $\mathbf{r}_1$ and $\mathbf{r}_2$ are two receivers. The main influencing factor in interferometric stacking is train speed v. The slower the decay of pier crosstalk factor H_n in stacking, the stronger the HSR coherence.

2.2 HSR Seismic Interferometry and Coherence Strength

Since HSR source timing is not precisely controllable, seismic interferometry is necessary to construct virtual sources. HSR seismic interferometry typically requires stacking numerous events to suppress source coherence. Related theoretical analysis suggests the primary de-coherence factor in stacking is train speed variation (Liu et al., 2021a; Yin et al., 2024). Consequently, HSR seismic interferometry can theoretically be expressed as:

$$\begin{aligned} C(\mathbf{r}_1,\mathbf{r}_2,\omega) &= \sum_v d(\mathbf{r}_1,\omega)d(\mathbf{r}_2,\omega)^* \\ &= \sum_v \sum_m \sum_n |S(\omega,v)|^2 G(\mathbf{r}_1|\mathbf{x}_s^m,\omega)G^*(\mathbf{r}_2|\mathbf{x}_s^n,\omega)\mathrm{e}^{-\mathrm{i}\omega(n-m)\frac{L}{v}} \\ &= \sum_m G(\mathbf{r}_1|\mathbf{x}_s^m,\omega)G^*(\mathbf{r}_2|\mathbf{x}_s^m,\omega)\cdot\sum_v |S(\omega,v)|^2 \sum_n \frac{G^*(\mathbf{r}_2|\mathbf{x}_s^n,\omega)}{G^*(\mathbf{r}_2|\mathbf{x}_s^m,\omega)}\mathrm{e}^{-\mathrm{i}\omega(n-m)\frac{L}{v}} \\ &= \sum_m G(\mathbf{r}_1|\mathbf{x}_s^m,\omega)G^*(\mathbf{r}_2|\mathbf{x}_s^m,\omega)\cdot C_m, \end{aligned} \tag{4}$$

where $\mathbf{r}_1, \mathbf{r}_2$ correspond to two station positions, $\mathbf{x}_s^m, \mathbf{x}_s^n$ are different pier source locations, and the term C_m represents the crosstalk caused by HSR coherence during stacking. C_m includes contributions not only from the m-th pier but also from neighboring piers, so that the pier sources are not independent — this is the unique coherence signature of HSR sources in seismic interferometry. The larger the contribution from neighboring piers, the stronger the coherence between pier sources.

Liu et al. (2021a), based on an assumption of large train speed variation, concluded that source coherence could be neglected, i.e., $C_m \sim 1$, achieving de-coherence. However, in actual HSR operations, speed distribution is concentrated; for 300 km/h-class trains, the speed standard deviation $\sigma_v \approx 2$ m/s, far from the theoretical assumption range (Jiang et al., 2019).

Under coherent conditions, although related studies suggest the phase influence of C_m can be neglected (Yin et al., 2024), its amplitude enhancement effect for different frequencies and azimuths will significantly alter VSG characteristics. This enhancement effect is related to contributions from adjacent piers and warrants quantitative analysis. Note that C_m can be approximated as:

$$C_m \approx \sum_n H_{n-m} \mathrm{e}^{-\mathrm{i}\omega(n-m)\tau_I(v_0)}, \tag{5}$$

where v_0 is the average train speed, and H_{n-m} represents the contribution factor of the n-th pier to the m-th pier source. The decay rate of H_{n-m} with $|n-m|$ reflects the coherence strength of the HSR source. For simplicity, assume $m = 0$, $H_n = H_{n-m}$.

To first order, we can simplify by ignoring wavelet spectral variations with train speed ($|S(\omega, v)|^2 = 1$) and letting $\tau_v = \frac{L}{v} - \frac{L}{v_0}$. Assuming a small speed variation range ($v_0 \pm \Delta V/2$), H_n can be approximated as:

$$\begin{aligned} H_n &= \sum_v |S(\omega, v)|^2 \mathrm{e}^{-\mathrm{i}\omega n \tau_v} \\ &\sim \frac{2\sin(\omega n \delta\tau_v/2)}{\omega n \delta\tau_v} \end{aligned} \tag{6}$$

As shown in Fig. 2, at low frequencies (e.g., the fundamental train frequency $f_c^1 \approx$ 3.3 Hz), the limited train speed variation range causes H_n to decay slowly; at least 13 neighboring piers ($|H_{|n|<6}| > 0.5$, $\sim$ 400 m) maintain considerable coherence. Coherence is effectively suppressed only at high frequencies (e.g., $f_c^3 \approx 9.9$ Hz) and under an assumption of extremely large speed variation, where $H_n \approx \delta(n)$.

Therefore, for actual HSR seismic data, even after seismic interferometry and multi-train stacking, inter-pier coherence characteristics are largely preserved rather than eliminated. This means the frequency and energy properties of the HSR source will still govern its VSG results, which is a fundamental premise for analyzing HSR VSG characteristics.

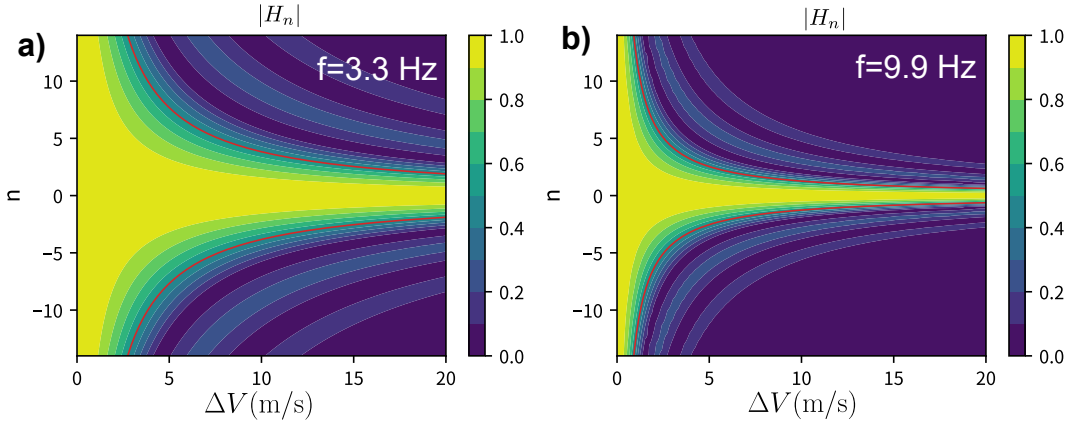


Figure 2. Distribution of pier crosstalk factors. Figures (a) and (b) show the pier crosstalk factor H_n versus pier separation n and speed variation range ΔV (v_0=83 m/s) at frequencies 3.3 Hz (f_c^1) and 9.9 Hz (f_c^3), respectively. The red contour marks $|H_n| = 0.5$. Results show that under an effective speed range $\Delta V = 6$ m/s, low-frequency coherence length can reach several hundred meters.

2.3 Theoretical Model of HSR Source Radiation Patterns

The analysis above shows that pier-to-pier coherence survives stacking, selectively amplifying certain frequency–azimuth combinations. To quantify this selectivity, combining Eqs. (2) and (4), HSR seismic interferometry can be expressed as:

$$\begin{aligned} C(\mathbf{r}_1, \mathbf{r}_2, \omega) &= G(\mathbf{r_1}|\mathbf{x}_s^0, \omega) G^*(\mathbf{r_2}|\mathbf{x}_s^0, \omega) \cdot \sum_v |S(\omega, v)|^2 A_1 A_2 \\ &= G(\mathbf{r_1}|\mathbf{x}_s^0, \omega) G^*(\mathbf{r_2}|\mathbf{x}_s^0, \omega) \cdot P, \end{aligned} \tag{7}$$

where $\mathbf{x}_s^0$ is the pier on the line connecting stations $\mathbf{r}_1$ and $\mathbf{r}_2$. The coherence of the HSR source is fully reflected in the azimuth and frequency distribution of P. If $P \approx 1$, the result depends only on the inter-station path difference, representing ideal seismic interferometry.

Based on this, we set $\mathbf{r}_1 = \mathbf{r}_2$ under far-field conditions and define $P(\theta, \omega; c)$ as the HSR radiation pattern. It represents the amplitude enhancement capability of the HSR source on the seismic interferometry result (VSG) for different frequencies and azimuths under a fixed medium wave velocity c, resulting from the coupling of the wavelet spectrum $|S|^2$ (dominated by train frequencies f_c^m) and the array interference factor A^2 (dominated by pier frequencies f_I^n):

$$P(\theta, \omega; c) = \sum_{v} |S(\omega, v)|^2 A(v, \omega, \theta; c)^2. \tag{8}$$

We obtain the specific form of the HSR radiation pattern via numerical simulation. Fifty-one pier sources spaced 32 m apart are excited sequentially according to train speed v. Receivers are placed on a circle with a radius of 8 km. Autocorrelation results for different speeds are stacked (Fig. S1), and the variations in frequency components and energy intensity across different azimuths constitute the HSR source radiation pattern. We choose two representative medium wave velocity: $c = 320$ m/s (shallow surface waves) and $c = 2500$ m/s (deep body waves). Results are shown in Figs. 3 and 4.

When the source wavelet is a δ wavelet ($|S(\omega, v)|^2 \equiv 1$), the HSR radiation pattern is controlled solely by pier interference, and radiated energy concentrates between the pier frequencies $f_I^n|_{v_{min}} \sim f_I^n|_{v_{max}}$ (Fig. 3 a and c). f_I^n shows clear variation with angle θ, and the lower the wave velocity, the more pronounced the frequency difference between the train front ($\theta = 0$) and rear ($\theta = \pi$).

When using a wavelet type closer to an actual train, where each wheel assembly excites a δ wavelet (Liu et al., 2021a; Jiang et al., 2022; L. Wang et al., 2025), the radiation pattern is jointly controlled by train frequencies f_c^m and pier frequencies f_I^n (Fig. 3 b and d). $P(\theta, \omega)$ resembles a multiplicative superposition of the two, exhibiting two bands in the spectrum. At the intersection of the two bands, radiation intensity is far stronger than from a single coherence effect (Fig. 4). Moreover, during multi-speed stacking, both f_c^m and f_I^n are positively correlated with train speed. This causes their intersection points to move primarily toward higher frequencies with increasing speed, concentrating in specific azimuths. The location of this intersection is closely related to wave velocity. For $c = 320$ m/s, representing surface wave velocity in loose sediments, the intersection mainly exists about 30 degrees ($\theta \approx \pi/6$) in front of the train (Fig. 3b and 4a). For $c = 2500$ m/s, a typical body wave velocity, energy is mainly concentrated in the train's rear hemisphere due to the intersection of f_c^3 and f_I^4 near the train's tail (Fig. 3d and 4b).

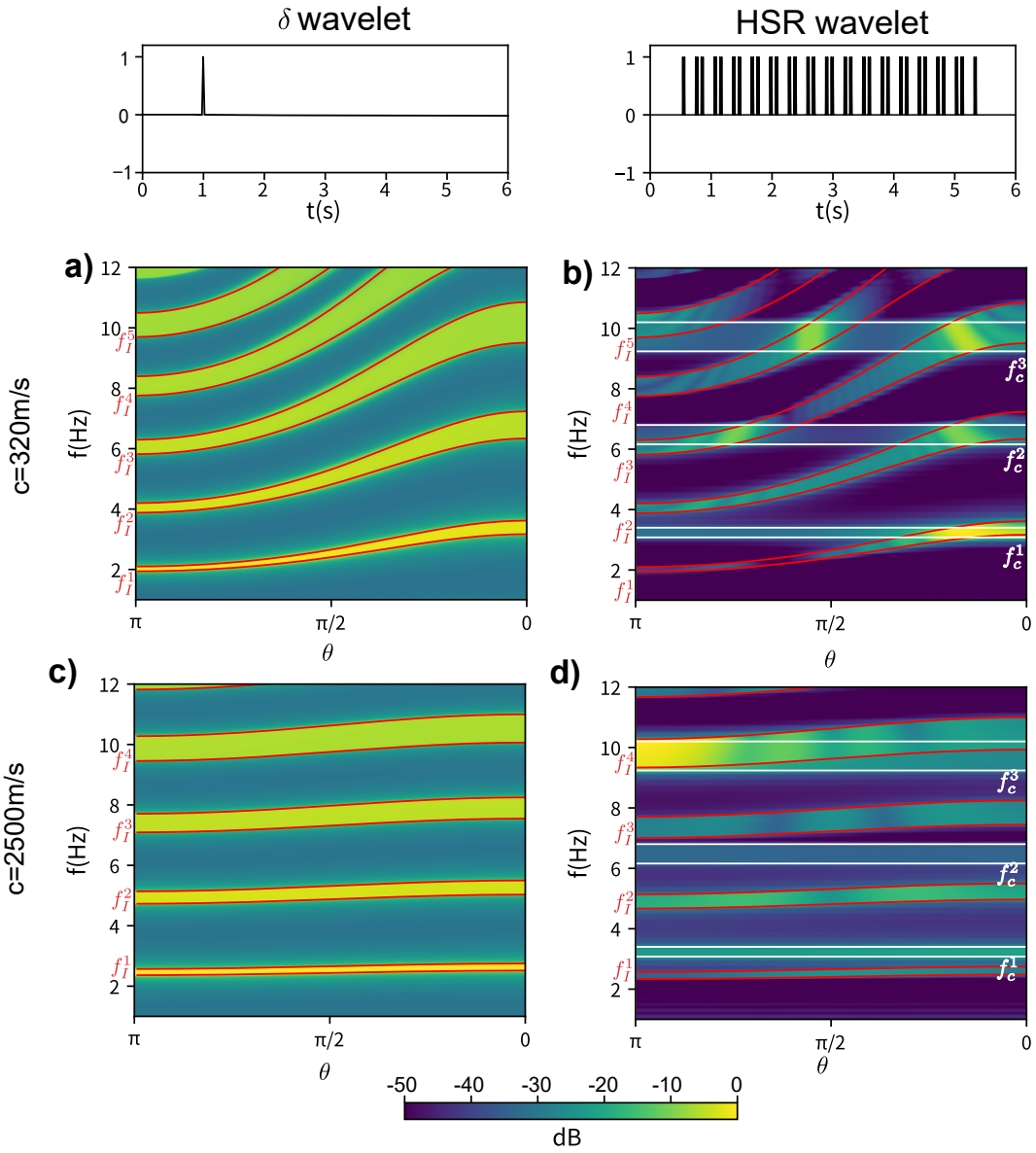


Figure 3. Simulated radiation patterns for different wavelets and wave velocities. (a, c) Pier wavelets are δ wavelets; medium wave velocities are 320 m/s and 2500 m/s, respectively. (b, d) Pier wavelets are HSR train wavelets. Red lines correspond to different orders of pier frequency f_I^n; white solid lines are multi-order train frequencies f_c^m. Upper and lower frequency limits of the same order are determined by train speeds v_{max} and v_{min}. In simulation, $\theta = 0$ is in front of the train, $\theta = \pi$ is behind (Fig 1). Train speed v is uniformly distributed within $[77, 85]$ m/s, and speed interval is 0.1 m/s. Train model: 16 carriages, carriage length 25 m, 4 wheelsets at [2.5, 5.0, 20.0, 22.5] m positions. $dB = 10\lg(P/P_{max})$. Wiggles are shown in Fig. S1.

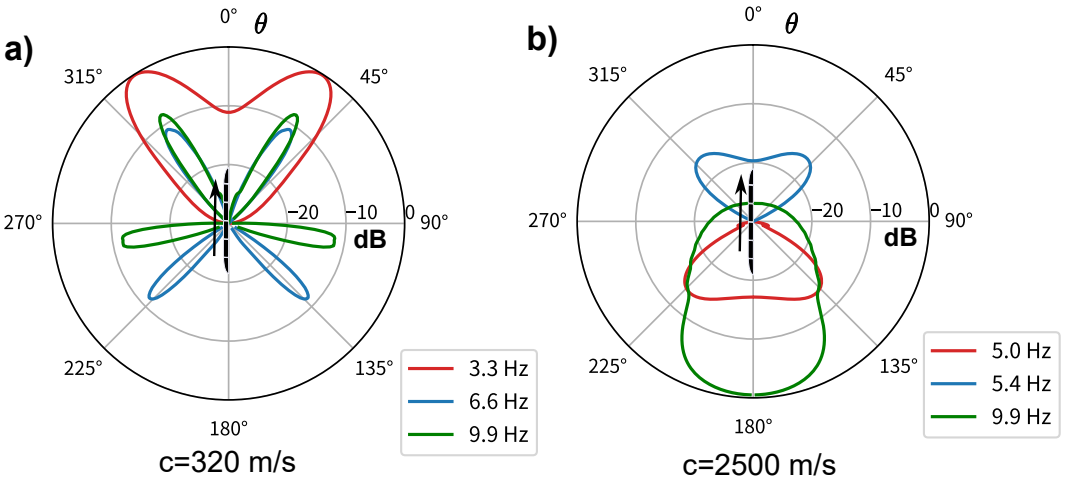


Figure 4. Simulated radiation patterns for different typical phases. (a) Simulated surface wave radiation pattern, wave velocity set to 320 m/s. (b) Simulated body wave radiation pattern, wave velocity 2500 m/s. Simulation parameters are the same as Fig. 3, using train wavelet. Speed v is normally distributed, $v \in N(83, 1.8)$ m/s. Different frequency components are indicated: 3.3 Hz and its harmonics are train frequencies; 5.0 Hz and 5.4 Hz are f_1^2-related frequencies. Spectrums are shown in Fig. S2.

3 Observations: Virtual Shot Gathers and Radiation Pattern Characteristics

In field data, HSR sources can generate different phases. Clarifying the radiation pattern characteristics of these phases within VSGs will aid in developing detection and monitoring methods tailored to phase attributes. Having analyzed the theoretical radiation patterns for different phase velocities, we now proceed to observational validation and examine the impact of different data processing methods on phase characteristics.

3.1 Data and Array

We conducted field observation around the Beijing-Guangzhou HSR in Wangdu County, Baoding City, in March 2023 (Fig. 5a). We used 160 Z-component nodal seismometers for three weeks. The observation area is centered on the Fujiaying Special Bridge, which has 349 piers mostly spaced at 32 m. At road crossings, a few spans are 24 m or 48 m. Both ends of the bridge are embankment sections. The array consists of multiple lines with intra-line station spacing of about 100 m. Many stations were deployed under the HSR line to collect train operation information.

To perform HSR seismic interferometry, we first searched for train events in the data. Using stations along the railway and prominent train vibration characteristics (Fig. S3), we identified over 5,400 train events, with a time distribution shown in Fig. 5b. Train density is roughly uniform from noon to midnight, peaking at 20 trains per hour, averaging one train every three minutes. A maintenance window from midnight to early morning results in very few train events for about 6 hours each day.

We then used receivers along the railway to extract arrival times of train events at different stations, fitting train position, direction, and speed information (Fig. S4). The speed distribution (Fig. 5c) shows three peaks corresponding to 250 km/h, 300 km/h, and 350 km/h speed classes. Trains are primarily 300 km/h-class, with speeds concentrated at 79$\sim$85 m/s and σ_v(300 km/h)=1.8 m/s, consistent with the realistic parameters used in our theoretical analysis.

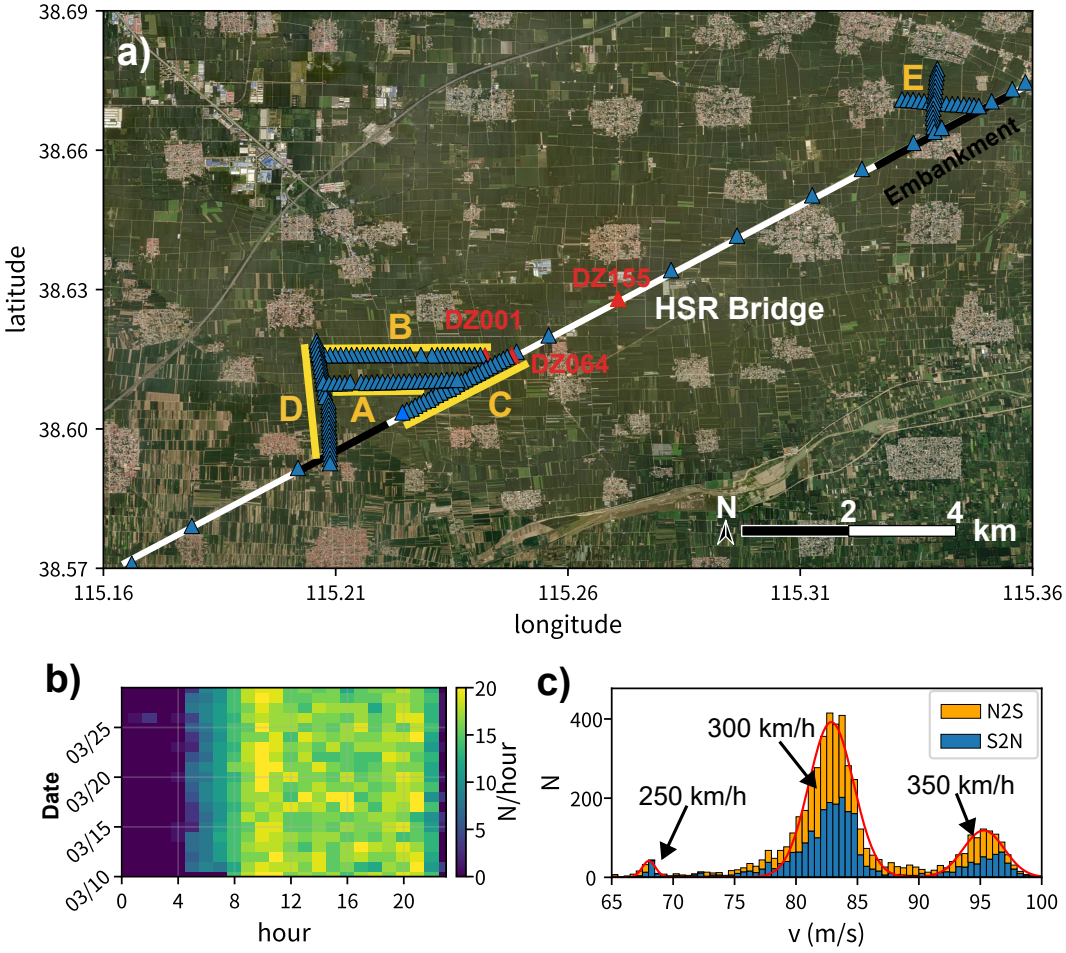


Figure 5. Array distribution and train event statistics. (a) Station distribution. Lines A, B, C, D have receiver spacing ∼100 m. Three red stars mark virtual source locations for seismic interferometry (DZ001, DZ064, DZ155). (b) Time distribution of train events during the observation period. (c) Speed distribution of train events: blue histogram for south-to-north (S2N) trains, orange for north-to-south (N2S) trains; combined histogram shows all trains. Red lines in (c) are fitted normal distributions, of which σ_v are 0.5/1.8/1.7 m/s for 250/300/350 km/h trains, respectively.

3.2 Radiation Pattern Characteristics of HSR Surface Waves

We employed Line B to construct VSGs for trains traveling in opposite directions, in order to characterize the radiation pattern of HSR surface waves. In the processing, events were first separated by travel direction into north-to-south (N2S) and south-to-north (S2N) groups. Because Line B makes an angle of roughly 35° with the HSR track, it lies in the forward hemisphere for N2S direction and in the rear hemisphere for S2N.

For each event, we selected a 15-s time window centered on the moment the train passed the intersection of Line B and the railway, extracted the recordings from all Line B stations, and cross-correlated each with the record of station DZ001. Before being stacked over events of the same direction to yield VSGs, the cross-correlation results were firstly subjected to pre-stack processing, either amplitude normalization or spectral whitening. Amplitude normalization is a global time-domain operation that mitigates the influence of anomalous amplitudes from individual events. Spectral whitening, a frequency-dependent normalization, balances the contributions of different events at all frequencies during stacking but can markedly enhance signals from other noise sources. Employing these distinct pre-stack processing schemes helps identify the energy levels and effective frequency components of seismic phases, and analyze their characteristics.

Fig. 6 shows the VSG obtained with amplitude normalization and spectral whitening when Line B is situated in the train's forward hemisphere. When the surface wave phase velocity in the 3–4 Hz band is approximately 320 m/s, the angle θ between Line B and the train's travel direction places the observation near the intersecting high-energy region of the train frequency f_c^1 and the pier frequency f_I^1 predicted by the theoretical radiation pattern (Fig. 3b and 4a). Consequently, this favorable azimuth strongly enhances the surface wave from HSR, making the HSR frequency component highly prominent in the Frequency–Celerity (FC) domain and manifesting predominantly as the train frequency f_c^1 characteristic of 300 km/h class trains (Fig. 6c). The signal of f_c^1 also exhibits good consistency across different events, so that it remains the dominant component after pre-stack spectral whitening (Fig. 6d). VSGs thus display pronounced HSR-dominant characteristics, consistent with the theoretical prediction.

In stark contrast, VSGs are markedly different when Line B lies in the train's rear hemisphere (Fig. 7). For a surface wave velocity of 320 m/s, the theoretical radiation pattern (Fig. 3b and 4a) predicts that the rear hemisphere cannot support the coherent superposition of f_c^1, placing this azimuth in a low-energy region. Consequently, while frequency components related to train frequencies remain visible in the VSG, their energy fails to concentrate near the surface wave dispersion curve (Fig. 7). After spectral whitening, the dominance shifts entirely to frequency components near 2.0 Hz, and the resulting spectral distribution closely resembles that of ambient noise interferometry (Fig. 7d and S5). Furthermore, the VSG exhibits pronounced non-causal arrivals (Fig. 7b) and lacks clear HSR-source-side dominance. These observations collectively indicate that

the signals in this configuration are dominated by ambient noise sources rather than HSR. This finding underscores that even when seismic interferometry is deliberately targeted at HSR sources, strong external noise interference inevitably dominates the result if the observation azimuth places the HSR frequency components in a low-energy region.

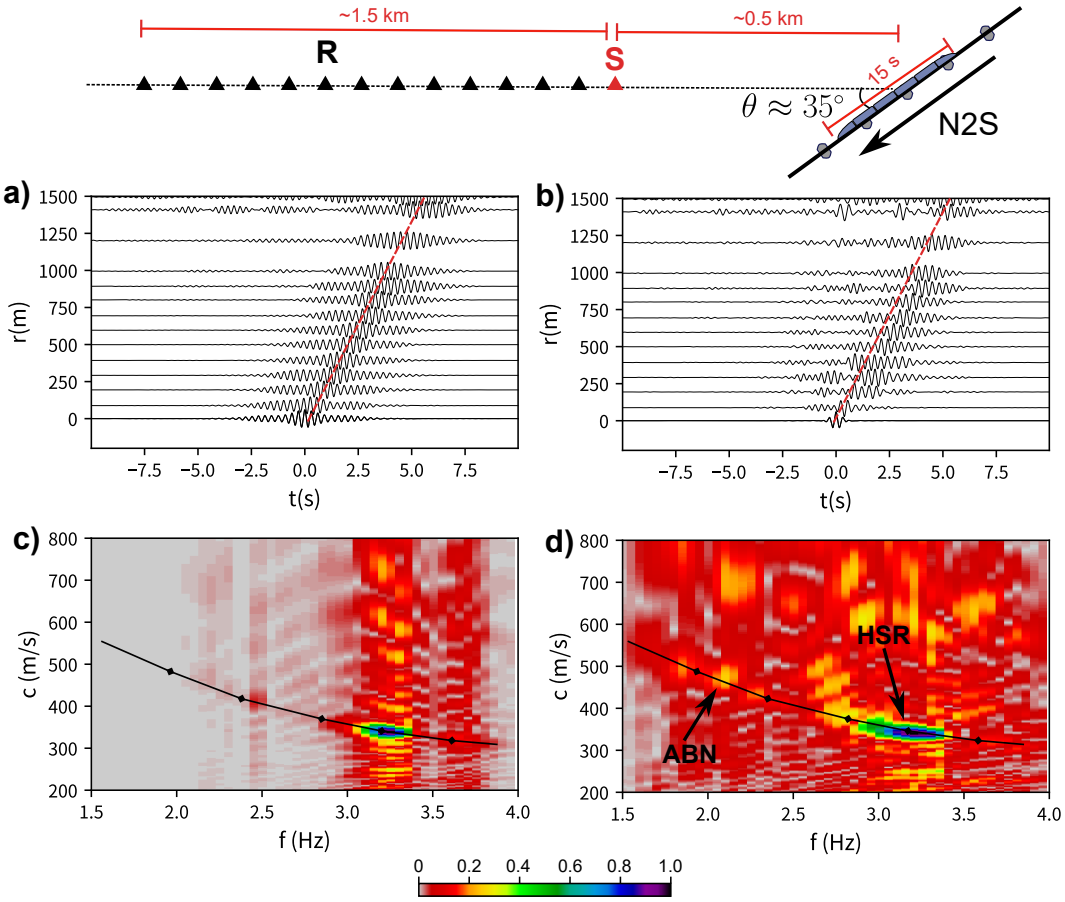


Figure 6. Surface waves in HSR VSGs when the line is located in the train's forward hemisphere. (a) Shot gather after pre-stack event amplitude normalization. (b) Shot gather after pre-stack spectral whitening. (c, d) FC-domain energy distribution of the shot gathers in (a) and (b), respectively. Black dotted lines mark the fundamental-mode surface wave dispersion curve. Energy near 2.0 Hz resembles that of ambient noise (ABN) (Fig. S5). VSGs are generated using Line B stations; the virtual source S is station DZ001.

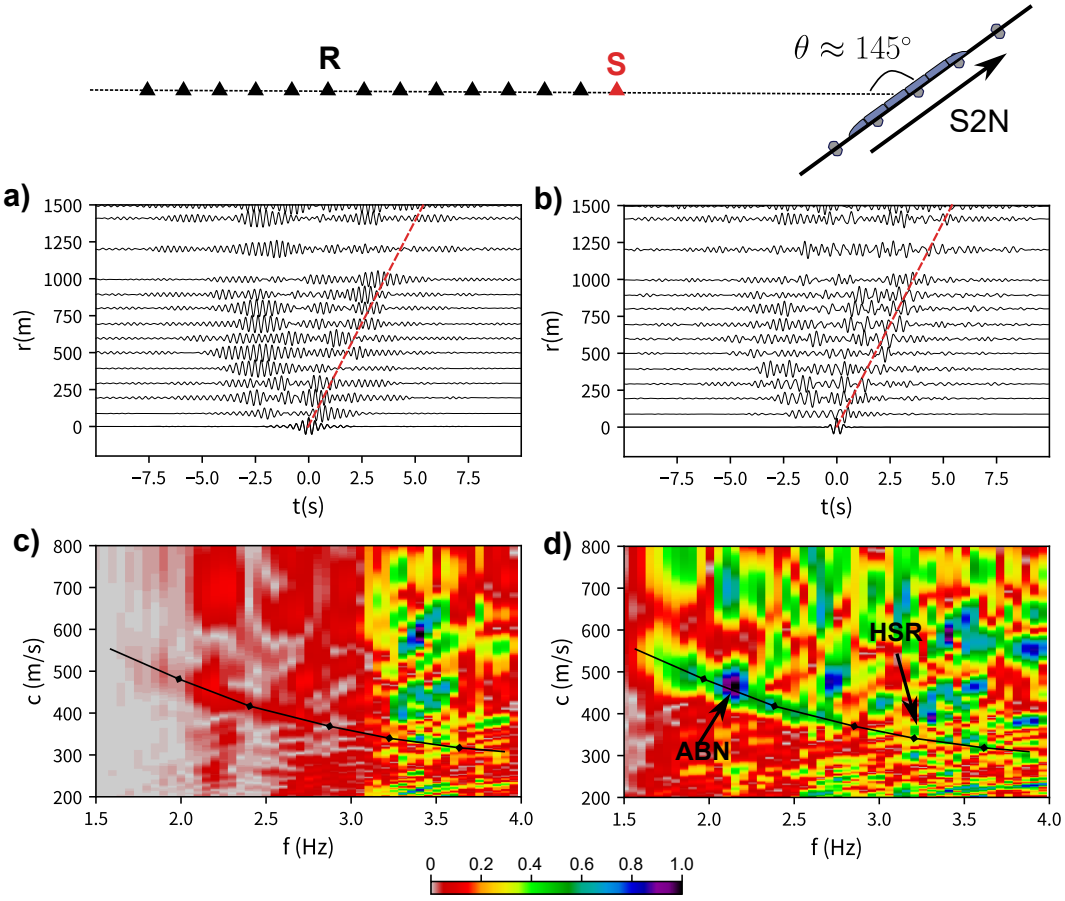


Figure 7. Surface waves in HSR VSGs when the line is located in the train's rear hemisphere. (a) Shot gather after pre-stack event amplitude normalization. (b) Shot gather after pre-stack spectral whitening. (c, d) FC-domain energy distribution of the shot gathers in (a) and (b), respectively. Black dotted lines in (c, d) mark the fundamental-mode surface wave dispersion curve. Energy components related to ambient noise (ABN) are indicated in (d) (see Fig. S5). VSGs are generated using Line B stations; the virtual source S is station DZ001.

3.3 High-Velocity Phase Along the Railway and Its Radiation Pattern

To further investigate the effect of HSR radiation patterns on VSGs, we analyzed seismic interferometry results along the railway (Line C). The Line C VSGs are dominated by a high-velocity seismic phase. As with the surface-wave phase observed on Line B, the frequency content of this phase depends on the train travel direction, exhibiting obvious radiation pattern characteristics.

Line C stations are situated directly beneath the HSR bridge; consequently, the relative azimuths assume only two values: $\theta = 0$ or π. Because the railway south of Line C lies on an embankment, we restrict our analysis to time windows during which trains are located north of line C. When the distance from the train to the line exceeds 3 km, 40-s records from Line C are selected for cross-correlation. The cross-correlation results undergo pre-stack spectral whitening; the stacked result, derived from approximately 5300 events, is presented in Fig. 8. The Line C VSG (Fig. 8a) reveals that this high-velocity phase has a group velocity of approximately 2000 m/s, whereas in the FC domain (Fig. 8b) its phase velocity exceeds 2500 m/s. The high-velocity phase is concentrated in two frequency bands: 5–7 Hz and 9–12 Hz. In the 5–7 Hz band, the phase velocity surpasses 3000 m/s, while at 10 Hz and above it decreases to roughly 2500 m/s, exhibiting clear dispersion.

To examine the radiation pattern of this phase, we further restricted the analysis to 300 km/h-class trains, thereby avoiding spectral complexity arising from the inclusion of multiple speed classes. VSGs for the two opposing directions of train motion are shown in Fig. 9. When the line lies ahead of the train ($\theta = 0$), the VSG energy peak resides above 5 Hz. When the line lies behind the train ($\theta = \pi$), the corresponding peak frequency decreases markedly, consistent with the azimuthal variation of the second-order pier frequency f_I^2 (Fig. 3d and 4b). Another notable feature is that energy near 10 Hz is nearly absent when the line is ahead of the train, yet prominent when the line is behind it. This behavior is consistent with the characteristic intersection of f_I^4 and f_c^3 behind the train for $c = 2500$ m/s (Fig. 3d and 4b). In addition, the high-velocity phase near 12.5 Hz exhibits a frequency shift with train direction, corresponding to the azimuthal variation of f_I^5. The energy at 6.5 Hz corresponds to f_c^2. Its amplitude suggests that f_c^2 may be enhanced by pier interference, possibly related to resonance between the limited number of 24-m piers and the 25-m carriages. The VSG displays an energy gap in the 7–10 Hz range and lacks the energy peak corresponding to f_I^3 near 7.5 Hz. This absence likely reflects the fact that actual HSR wavelets carry little energy in this band under wheelset modulation (Jiang et al., 2022).

With respect to the relative amplitudes of different frequency components, some discrepancies from the simulated radiation pattern are observed: for instance, the energy at f_I^2 exceeds that at f_c^3. We attribute this primarily to attenuation in the real data; when the line is far from the train, high-frequency components decay more rapidly, sup-

pressing the f_c^3 energy. Furthermore, all VSGs presented here underwent pre-stack spectral whitening and stacking, thereby discarding the original amplitude information and diminishing the amplitude-enhancement effect of the radiation pattern. When trains are closer to the line and pre-stack whitening is omitted, high-frequency components in the HSR VSG become more prominent, and the f_c^3 energy surpasses that at f_I^2 (Fig. S6). On the whole, the frequency distribution and azimuthal dependence observed in the Line C VSGs are broadly consistent with the theoretical radiation pattern.

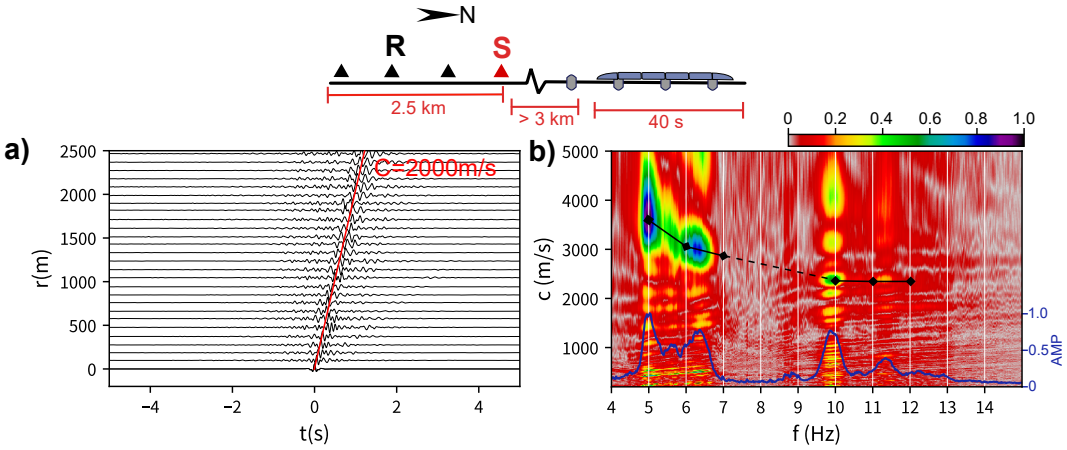


Figure 8. VSG obtained from trains concentrated north of Line C, in the 4–15 Hz frequency range. (a) VSG from Line C seismic interferometry; virtual source is DZ064; pre-stack spectral whitening has been applied. The red line marks a group velocity of 2000 m/s. (b) FC-domain energy distribution of the VSG. The blue curve shows relative amplitude as a function of frequency; the black dotted line is the high-velocity-phase dispersion curve, picked on the basis of spectral peak positions.

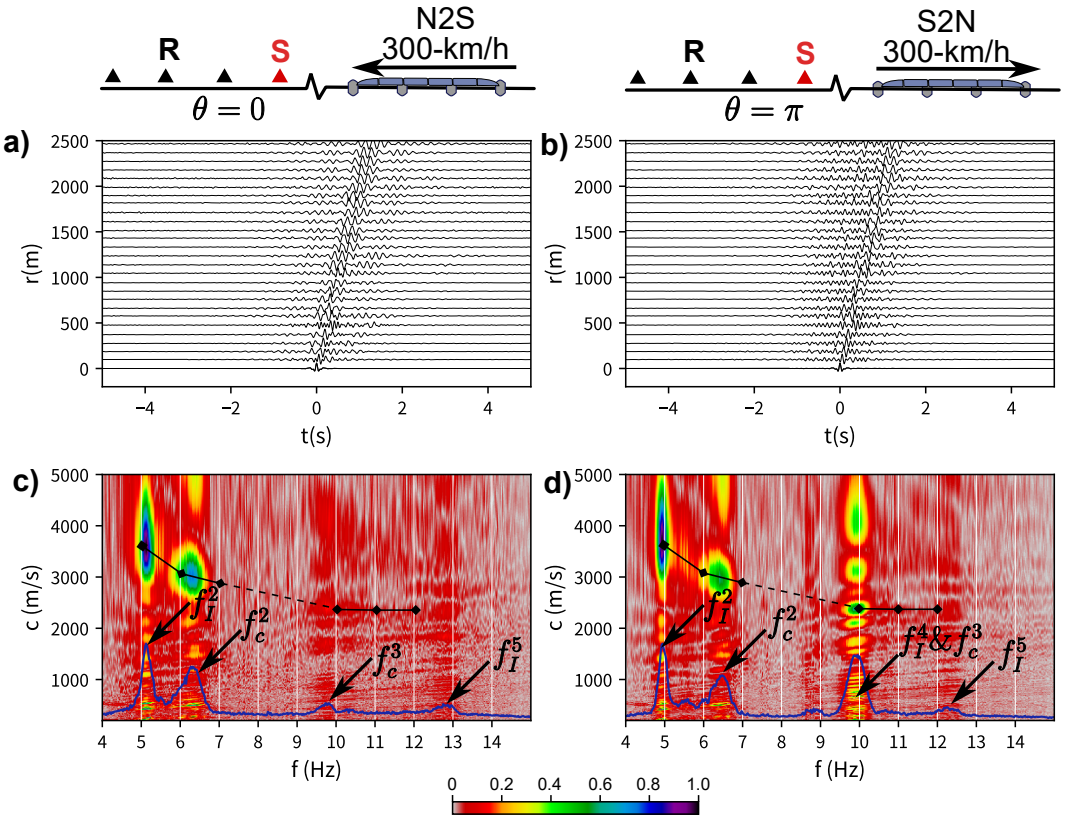


Figure 9. Effect of train motion direction on Line C VSGs. (a) VSG for N2S-directed 300 km/h-class train events. (b) VSG for S2N-directed events. In (a) and (b), the line is at azimuths of 0° and 180° relative to the train, respectively. Seismic interferometry parameters are the same as in Fig. 8. (c, d) FC-domain energy distribution of the shot gathers shown in (a) and (b), with the corresponding spectral orders indicated at each peak. Blue curves show relative energy as a function of frequency; black dotted lines mark the high-velocity-phase dispersion curve.

4 Discussion

4.1 Source of Low-Frequency Surface Waves Along HSR Lines

Current near-surface detection studies based on HSR sources often assume that deploying arrays along the railway can directly capture train-generated surface wave signals (Shao et al., 2022; Mi & Xia, 2023; Chang et al., 2025). From the perspective of incoherent noise sources, this view assumes that the train source lies within the stationary-phase zone of the line and that surface waves are therefore naturally dominated by the train. However, our results (Figs. 2 and 7) demonstrate that when the line azimuth falls within a low-energy region of the HSR radiation pattern, surface waves in the VSG may

be dominated by ambient noise, even when seismic interferometry is deliberately targeted at HSR sources. In our study area, HSR-generated surface waves are concentrated in the $\pi/6$ direction ahead of the train (Figs. 3b and 6), raising a key question: Are the low-frequency surface waves extracted by along-track seismic interferometry truly dominated by the HSR source?

To resolve this question of energy attribution, we conducted a comparative analysis using Line C. Unlike fixed noise sources such as highways, the relative azimuth of the train source can be systematically varied by selecting appropriate time windows. By selecting records in which trains are located at either end of the line for cross-correlation and stacking, we construct variant VSGs (Fig. 10). When trains are north of the line, the VSG exhibits three prominent phases (Fig. 10a); combined with the FC-domain energy distribution (Fig. 10c), these can be identified as fundamental-mode surface waves, higher-mode surface waves, and the aforementioned high-velocity seismic phase. Among these, although the high-velocity phase is less spatially continuous than at higher frequencies (Figs. 8 and 9), its frequency band coincides with the HSR source characteristic frequency f_c^1 and varies with the train's relative position, confirming that it is directly excited by the HSR source.

The surface wave signals, however, behave quite differently. They are concentrated below 3 Hz and show little dependence on HSR azimuth (Fig. 10b). Even when trains occupy the anti-causal position (south side), the VSG remains dominated by signals in the causal position ($t > 0$), and their spectral characteristics closely resemble those of pure ambient-noise interferometry results (Fig. S5). This evidence strongly indicates that, in the 1.5–4 Hz band, the surface waves extracted via along-rail interferometry are not HSR-dominated. Rather, they are governed by a persistent external noise source situated to the north of the line. Given their spectral similarity, they may share a common origin with the ambient-noise surface waves observed on Line B (Figs. 6d and 7d). At higher frequencies, surface wave energy is weak and far lower than that of the high-velocity phase (Fig. 8a). A comparison of Figs. 8 and 10 reveals that, in along-rail VSGs, the dominant contribution of the HSR source is the high-velocity phase, not surface waves.

This finding highlights the constraint that HSR radiation patterns impose on seismic interferometry. For a kilometer-scale array operating in the sub-4 Hz band, placement within a low-energy region of the radiation pattern means that surface waves along

the railway remain dominated by external sources, even when train time windows are carefully selected for train events. This underscores an important methodological point: under the influence of HSR source coherence, any attempt to exploit railway-generated seismic phases for subsurface detection and monitoring has to first establish the signal generation mechanism with reference to the radiation pattern morphology and the direction of coherent energy, and account for the contribution of external noise sources.

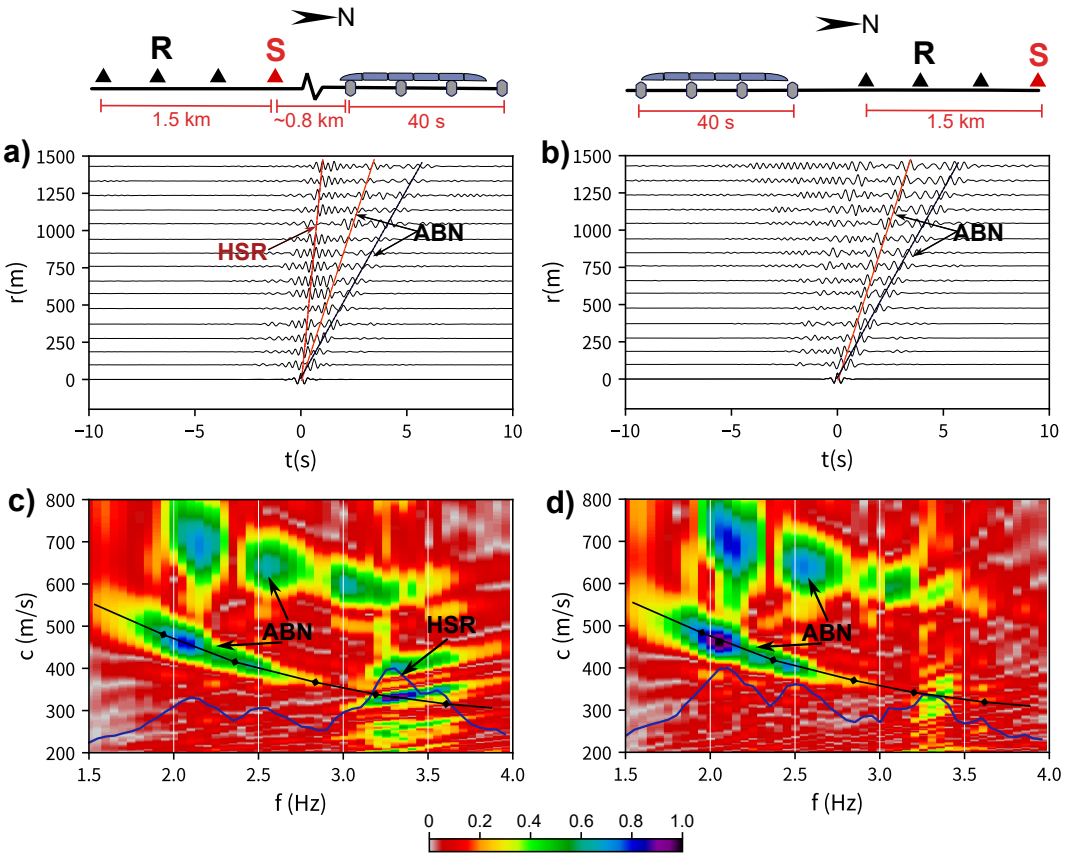


Figure 10. VSGs on Line C for different train azimuths. (a) VSG obtained when trains are north of Line C. (b) VSG obtained when trains are south of the stations on Line C. (c, d) Energy distribution in the 200–800 m/s velocity range for (a) and (b), respectively. The three diagonal lines in (a) and (b) mark velocities of approximately 250 m/s, 500 m/s, and 1500 m/s. The shot gathers are band-limited to 1.5–4 Hz. Virtual source is station DZ064; only a subset of Line C stations serve as receivers. Original record length is 40 s; each stack comprises about 2000 train-event cross-correlations; pre-stack spectral whitening was applied.

4.2 Formation Mechanism of the High-Velocity Phase

Observations in other regions have also detected high-velocity signals similar to this phase excited by HSR sources, which have been interpreted as deep refracted or diving P-waves (Jiang et al., 2022; Mi & Xia, 2023). Our results show that this phase additionally exhibits significant radiation-pattern and dispersion characteristics and constitutes the dominant component of along-track VSGs. To better exploit this phase for subsurface detection and monitoring along the railway, its specific propagation path and formation mechanism warrant detailed discussion.

First, the presence of this high-velocity phase away from the railway line provides critical evidence that it is a seismic wave (Fig. 11). When off-rail Lines A, B, and D are combined with along-rail Line C for seismic interferometry, the resulting VSG contains two dominant frequencies, f_I^2 and f_c^3 (Fig. 11c and Fig. S7). At comparable distances, the VSG formed by off-rail lines is highly consistent with that from along-rail Line C, and the same phase naturally extends to a distance of 6.5 km (Fig. 11b). This demonstrates that the propagation of the high-velocity phase does not depend on the railway line; it should be classified as a body wave or guided wave.

To further exclude the possibility that this signal originates from bridge structural vibrations, we examine two candidate wave types that could conceivably propagate along the bridge. If we ignore the periodic pier supports and treat the bridge as a continuous rod, guided waves are theoretically possible (Lamb, 1917; Rose, 2014). However, such guided waves are more commonly observed on horizontal components, and when the wavelength greatly exceeds the bridge width, only the anti-dispersive S0 and non-dispersive A0 modes exist, which is inconsistent with the normal dispersion we observe on the vertical component. Moreover, if the signal were a flexural wave in a periodically supported bridge (Mead, 1970), its propagation would be governed by passband and stopband characteristics imposed by the periodic boundary conditions. For a typical 32-m simply-supported HSR beam with a fundamental natural frequency of 6.0 Hz (S. Hu et al., 2013), frequencies below 6.0 Hz lie in a stopband, and the first passband above it is anti-dispersive (Xiao et al., 2013; Carta et al., 2017). Both properties contradict our observations (Fig. 8). We therefore conclude that the high-velocity phase is unrelated to typical bridge structural waves.

Given that its velocity approaches typical P-wave speeds and that it exhibits pronounced dispersion, this phase may correspond to a specific mode of guided-P waves (Nakata et al., 2015; H. Li et al., 2018; C. Shi et al., 2025). Its frequency characteristics are strongly correlated with the HSR source radiation pattern, further supporting a subsurface origin.

A comparison of along-rail and off-rail seismic interferometry results (Figs. 8 and 11) reveals, however, that the dispersion characteristics are not completely identical. When off-rail stations from Lines A, B, and D are included, the average phase velocity at 5 Hz is only 3000 m/s, not the 3500 m/s obtained for along-rail Line C alone (Figs. 8b and 11c), a difference possibly attributable to lateral heterogeneity in the guided-P wave velocity structure. Overall, fundamental attributes of this phase, such as its subsurface propagation path, still require determination through forward modeling constrained by additional data.

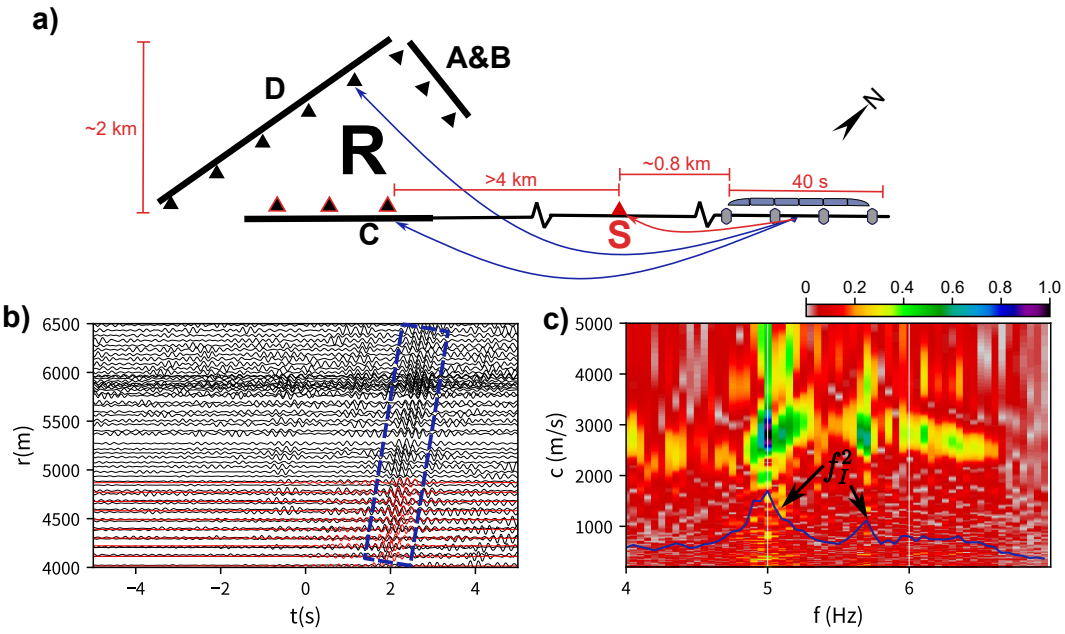


Figure 11. HSR seismic interferometry results using multiple receiver lines. (a) Schematic illustrating the principle of HSR seismic interferometry. The virtual source is station DZ155; receivers comprise along-rail Line C and off-rail Lines A, B, and D; r denotes the station-to-virtual-source distance. (b) VSG within 4–7 Hz. Black traces correspond to stations on Lines A, B, and D; red traces are from Line C stations. (c) FC-domain energy distribution of (b). Peaks near 5 Hz and 5.7 Hz correspond to the pier frequency f_I^2 for 300 km/h and 350 km/h-class trains, respectively. The VSG over a wider frequency range is shown in Fig. S7.

4.3 Implications of Radiation Patterns for HSR Source Monitoring Applications

As noted in the introduction, the overarching objective of HSR source studies is to develop a more efficient and repeatable monitoring source. Our results demonstrate that HSR sources are not isotropic random noise sources; rather, the source coherence that produces the radiation patterns concentrates energy into narrow frequency bands and specific azimuths, imparting directional radiation characteristics reminiscent of radar. This physical characteristic, in our view, endows HSR sources with strong theoretical potential for high-temporal-resolution seismic monitoring.

A first application is the monitoring of shallow subsurface media around the railway, leveraging the radiation pattern of HSR-generated surface waves. For typical surface waves propagating in soft sedimentary layers, the HSR source focuses energy in specific directions within the forward hemisphere of the train, producing a high-energy surface-wave beam that is observable within approximately 1 km of the railway (Fig. 6). These surface-wave signals possess an effective wavelength of roughly 100 m and are sensitive to subsurface velocity and density variations down to approximately 50 m depth. They can therefore be used to monitor environmental changes such as groundwater level fluctuations and shallow moisture content, with potential applications in agriculture, railway embankment settlement assessment, and related fields. If stable surface-wave signals can be extracted from a small number of HSR events, the temporal resolution of such monitoring could reach sub-hourly levels.

A second application exploits the radiation-enhanced high-velocity phase for railway foundation health monitoring. As the dominant signal along the railway direction, uniquely amplified by the HSR radiation pattern, the high-velocity phase remains clearly detectable at distances exceeding 6 km (Fig. 11), underscoring its potential for monitoring deep railway foundation conditions. As with surface waves, the high-velocity phase exhibits measurable dispersion, with wavelengths ranging from 250 m to 700 m and energy concentrated in several distinct frequency components (Figs. 8 and 9); monitoring results derived from different frequency components are therefore likely to reflect velocity changes at different depths.

Therefore, the practical deployment of HSR sources for monitoring follows directly from the radiation pattern geometry. For shallow subsurface imaging, arrays should be

placed in the forward hemisphere of the train and tuned to the f_c^1 frequency band. For deep foundation assessment, arrays should be aligned along the railway and targeted at the specific pier-frequency bands that dominate the high-velocity phase. This strategy replaces empirical event selection with physics-guided experimental design, maximizing the inherent coherence and energy advantages of HSR sources.

5 Conclusion

In summary, the dual coherence of HSR sources, arising from repeating train geometry and equally spaced bridge piers, is not eliminated by the stacking process of seismic interferometry. Instead, it imprints a persistent radiation pattern onto virtual shot gathers (VSGs). This radiation pattern is not a processing artifact to be removed; it is the physical basis that makes direction-resolved monitoring with HSR signals possible. We therefore conclude that HSR sources should be treated not as isotropic noise to be suppressed, but as directional radiators whose azimuthally selective energy can be strategically exploited.

The radiation pattern governs all HSR-generated phases through a common mechanism of azimuthal selectivity, yet produces sharply contrasting effects for different wave types. Surface-wave energy is focused into a narrow forward beam, producing strong signals usable for shallow monitoring, whereas outside this favored azimuth it collapses and is replaced by ambient noise. Body-wave energy is channeled into a dispersive high-velocity phase along the track that propagates well beyond the railway corridor, confirming its nature as a seismic signal suitable for deep probing. These two regimes define complementary monitoring pathways — shallow illumination ahead of the train and deep sounding along the track — both governed by the same underlying radiation-pattern physics and both exploitable once the pattern is theoretically understood.

Two open questions define the immediate next steps. First, the near-total absence of the predicted f_I^3 energy ($\sim$7.5 Hz) in field data indicates that current source-wavelet models, which treat the train and bridge as kinematically decoupled, are incomplete; incorporating dynamic train–bridge coupling should improve spectral predictions across all frequency bands. Second, the precise nature of the high-velocity phase — whether a specific guided-P mode, a deep refracted arrival, or a leaky surface-wave harmonic — remains unresolved. Three-dimensional forward modeling, combined with active-source

calibration, would clarify its identity and unlock its depth-sensitivity kernel for quantitative velocity-change monitoring at depth. Addressing these two issues will advance the HSR radiation pattern from a validated concept to an operational monitoring tool.

Data Availability Statement

The seismic data (including cross-correlation and stacked virtual shot gathers) and all processing scripts used in this study have been deposited at Zenodo (Y. Shi et al., 2026a, 2026b). Data processing was performed using ObsPy (Krischer et al., 2015), and figures were produced using Matplotlib (Hunter, 2007).

Author Contributions

- **Yongxiang Shi**: Developed the theoretical model of HSR coherence and performed numerical validation; processed and analyzed observational data characteristics; conducted data visualization and interpretation; wrote the manuscript.
- **Jingchong Wen**: Organized field data acquisition; contributed to the development and validation of the theoretical model; revised the manuscript.
- **Han Wu**: Contributed to the development and validation of the theoretical model; revised the manuscript.
- **Zhiyuan Zhao**: Led field data acquisition.
- **Ling Chen**: Contributed to project leadership; revised the manuscript.
- **Jieyuan Ning**: Contributed to project leadership; revised the manuscript.

Acknowledgments

This study utilized the HSR source wavelet provided by Dr. Yiran Jiang from Harbin Institute of Technology. Dr. Yiran Jiang and Dr. Zhichao Yu from the Institute of Geology and Geophysics, Chinese Academy of Sciences, participated in academic discussions related to HSR observational data and phenomenon interpretation, providing many valuable suggestions and directions for improvement. We thank Geo-DeepSensing Company and Professor Chuan He of Peking University for instrument support. We sincerely thank Academician Rixiang Zhu of the Institute of Geology and Geophysics, Chinese Academy of Sciences, for his support of HSR source research. This study was completed with sup-

port from the project "Theory of Hydrocarbon Enrichment under Multi-Spheric Interactions" (THEMSIE04010101).

Conflict of Interest Statement

The authors have no conflicts of interest to disclose.

References

Behm, M., & Snieder, R. (2013). Love waves from local traffic noise interferometry. *The Leading Edge*, *32*(6), 628–632. doi: 10.1190/tle32060628.1

Brenguier, F., Boué, P., Ben-Zion, Y., Vernon, F., Johnson, C., Mordret, A., … Lecocq, T. (2019). Train Traffic as a Powerful Noise Source for Monitoring Active Faults With Seismic Interferometry. *Geophysical Research Letters*, *46*(16), 9529–9536. doi: 10.1029/2019GL083438

Brenguier, F., Courbis, R., Mordret, A., Campman, X., Boué, P., Chmiel, M., … Hollis, D. (2020). Noise-based ballistic wave passive seismic monitoring. Part 1: Body waves. *Geophysical Journal International*, *221*(1), 683–691. doi: 10.1093/gji/ggz440

Carta, G., Giaccu, G., & Brun, M. (2017). A phononic band gap model for long bridges. The 'Brabau' bridge case. *Engineering Structures*, *140*, 66–76. doi: 10.1016/j.engstruct.2017.01.064

Chang, W., Shao, G., Liu, X., Huo, K., Wu, H., & Tan, C. (2025). A novel seismic interferometry method for high-speed train-induced vibrations based on deconvolution and weighted stacking. *Geophysics*, *90*(5), Q21-Q31. doi: 10.1190/geo2024-0845.1

Chen, Q., Li, l., Li, G., Chen, L., Peng, W., Tao, Y., … Wang, F. (2004). Seismic features of vibration induced by train. *Acta Seismologica Sinica (In Chinese)*, *26*(6), 651–659. doi: 10.3321/j.issn:0253-3782.2004.06.011

Cheng, F., Xia, J., Wang, B., & Zhang, C. (2025). Unveiling coastal dynamics using telecommunication fiber optic cables. *Science Bulletin*, *70*(12), 1945–1948. doi: 10.1016/j.scib.2025.02.023

Cunha Teixeira, J., Bodet, L., Rivière, A., Hallier, A., Gesret, A., Dangeard, M., … Boisson Gaboriau, J. (2025). Physics-Guided Deep Learning Model for Daily Groundwater Table Maps Estimation Using Passive Surface-

Wave Dispersion. *Water Resources Research*, *61*(1), e2024WR037706. doi: 10.1029/2024WR037706

Hong, Y., Mi, B., Chen, X., Zhang, H., & Guan, B. (2024). Near-surface imaging by joint analysis of traffic-induced Rayleigh and Love waves using 3C dense linear arrays: A case study in Hangzhou, China. *Journal of Applied Geophysics*, *222*, 105317. doi: 10.1016/j.jappgeo.2024.105317

Hu, G., Zhang, G., Sun, S., Li, Y., Yang, J., Duan, J., … Zhan, Y. (2019). Fwi of high-speed-train seismic first arrival signal. *Chinese Journal of Geophysics (in Chinese)*, *62*(12), 8. doi: 10.6038/cjg2019N0163

Hu, S., Niu, B., Ke, Z., & Liu, X. (2013). Study on the optimization of standard span length simply supported box girder for high-speed railway. *China Railway Science(in Chinese)*(1), 15–21. doi: 10.3969/j.issn.1001-4632.2013.01.03

Hung, H. H., & Yang, Y.-B. (2001). Elastic waves in visco-elastic half-space generated by various vehicle loads. *Soil Dynamics and Earthquake Engineering*, *21*(1), 1–17. doi: 10.1016/S0267-7261(00)00078-6

Hunter, J. D. (2007). Matplotlib: A 2d graphics environment. *Computing in Science & Engineering*, *9*(3), 90–95. doi: 10.1109/MCSE.2007.55

Jiang, Y., Bao, T., Ning, J., & Zhang, X. (2019). Spectral characteristics of high-speed rail seismic signal under viaduct. *Acta Scientiarum Naturalium Universitatis Pekinensis (in chinese)*, *55*(5), 829–838. doi: 10.13209/j.0479-8023.2019.072

Jiang, Y., Ning, J., Wen, J., & Shi, Y. (2022). Doppler effect in high-speed rail seismic wavefield and its application. *Science China Earth Sciences*. doi: 10.1007/s11430-021-9843-0

Krischer, L., Megies, T., Barsch, R., Beyreuther, M., Lecocq, T., Caudron, C., & Wassermann, J. (2015). ObsPy: a bridge for seismology into the scientific Python ecosystem. *Computational Science & Discovery*, *8*(1), 014003. doi: 10.1088/1749-4699/8/1/014003

Lamb, H. (1917). On waves in an elastic plate. *Proceedings of the Royal Society of London. Series A, Containing Papers of a Mathematical and Physical Character*, *93*(648), 114–128. doi: 10.1098/rspa.1917.0008

Lavoué, F., Coutant, O., Boué, P., Pinzon-Rincon, L., Brenguier, F., Brossier, R., … Bean, C. J. (2021). Understanding Seismic Waves Generated by Train Traffic

via Modeling: Implications for Seismic Imaging and Monitoring. *Seismological Research Letters*, *92*(1), 287–300. doi: 10.1785/0220200133

Li, H., Yang, W., & Yong, X. (2018). Deep learning for ground-roll noise attenuation. In *SEG Technical Program Expanded Abstracts 2018* (pp. 1981–1985). Society of Exploration Geophysicists. doi: 10.1190/segam2018-2981295.1

Li, L., Peng, W., Li, G., Chen, Y., Chen, Q., & Tang, Y. (2004). Induced by trains: A new seismic source and relative test. *Chinese Journal of Geophysics (in Chinese)*, *47*(4), 680–684.

Liu, Y., Yue, Y., Luo, Y., & Li, Y. (2021a). Effects of high-speed train traffic characteristics on seismic interferometry. *Geophysical Journal International*, *227*(1), 16–32. doi: 10.1093/gji/ggab205

Liu, Y., Yue, Y., Luo, Y., & Li, Y. (2021b). The seismic broad-band signature of high-speed trains running on viaducts. *Geophysical Journal International*, *226*(2), 884–892. doi: 10.1093/gji/ggab144

Mao, S., Ellsworth, W. L., Zheng, Y., & Beroza, G. C. (2025). Depth-dependent seismic sensing of groundwater recovery from the atmospheric-river storms of 2023. *Science*, *387*(6735), 758–763. doi: 10.1126/science.adr6139

Mead, D. (1970). Free wave propagation in periodically supported, infinite beams. *Journal of Sound and Vibration*, *11*(2), 181–197. doi: 10.1016/S0022-460X(70)80062-1

Meng, Y., & Liu, Z. (2025). Review of temporal variations of underground medium based on seismic waves. *Reviews of Geophysics and Planetary Physics (in Chinese)*, *56*(3), 292–312. doi: 10.19975/j.dqyxx.2024-027

Mi, B., & Xia, J. (2023). Extraction of Rayleigh, Love, and Virtual Refraction Waves From 3C High-Speed-Train-Induced Vibrations for Near-Surface Characterization. *IEEE Transactions on Geoscience and Remote Sensing*, *61*, 1–10. doi: 10.1109/TGRS.2023.3318989

Mi, B., Xia, J., Tian, G., Shi, Z., Xing, H., Chang, X., … Zhang, H. (2022). Near-surface imaging from traffic-induced surface waves with dense linear arrays: An application in the urban area of Hangzhou, China. *Geophysics*, *87*(2), B145-B158. doi: 10.1190/geo2021-0184.1

Mi, B., Xia, J., Xu, Y., You, B., & Chen, Y. (2023). Retrieval of surface waves from high-speed-train-induced vibrations using seismic interferometry. *Geophysics*,

88(5), KS113-KS126. doi: 10.1190/geo2022-0603.1

Mordret, A., Courbis, R., Brenguier, F., Chmiel, M., Garambois, S., Mao, S., … Hollis, D. (2020). Noise-based ballistic wave passive seismic monitoring – Part 2: Surface waves. *Geophysical Journal International*, *221*(1), 692–705. doi: 10.1093/gji/ggaa016

Mukherjee, S., Li, Y. E., Stumpf, A., & Zhang, H. (2026). Monitoring Near-Surface Changes Using Anthropogenic Seismic Vibrations. *Geophysical Research Letters*, *53*(6), e2025GL120455. doi: 10.1029/2025GL120455

Nakata, N., Chang, J. P., Lawrence, J. F., & Boué, P. (2015). Body wave extraction and tomography at Long Beach, California, with ambient-noise interferometry. *Journal of Geophysical Research: Solid Earth*, *120*(2), 1159–1173. doi: 10.1002/2015JB011870

Nakata, N., Snieder, R., Tsuji, T., Larner, K., & Matsuoka, T. (2011). Shear wave imaging from traffic noise using seismic interferometry by cross-coherence. *GEOPHYSICS*, *76*(6), SA97-SA106. doi: 10.1190/geo2010-0188.1

Quiros, D. A., Brown, L. D., & Kim, D. (2016). Seismic interferometry of railroad induced ground motions: Body and surface wave imaging. *Geophysical Journal International*, *205*(1), 301–313. doi: 10.1093/gji/ggw033

Rose, J. L. (2014). *Ultrasonic guided waves in solid media*. Cambridge university press.

Shao, J., Wang, Y., & Chen, L. (2022). Near-Surface Characterization Using High-Speed Train Seismic Data Recorded by a Distributed Acoustic Sensing Array. *IEEE Transactions on Geoscience and Remote Sensing*, *60*, 1–11. doi: 10.1109/TGRS.2022.3153831

Shen, Z., Yang, Y., Fu, X., Adams, K. H., Biondi, E., & Zhan, Z. (2024). Fiber-optic seismic sensing of vadose zone soil moisture dynamics. *Nature Communications*, *15*(1), 6432. doi: 10.1038/s41467-024-50690-6

Sheng, Y., Mordret, A., Sager, K., Brenguier, F., Boué, P., Rousset, B., … Ben-Zion, Y. (2022). Monitoring Seismic Velocity Changes Across the San Jacinto Fault Using Train-Generated Seismic Tremors. *Geophysical Research Letters*, *49*(19), e2022GL098509. doi: 10.1029/2022GL098509

Shi, C., Li, Z., & Chen, X. (2025). Advances in the research of seismic-wave leaky modes. *Reviews of Geophysics and Planetary Physics (in Chinese)*, *56*(1), 1–

651 25. doi: 10.19975/j.dqyxx.2024-005

652 Shi, Y., Wen, J., & Ning, J. (2022). Theoretical analysis of high-speed rail seismic
653 imaging. *Science China Earth Sciences*. doi: 10.1007/s11430-021-9840-x

654 Shi, Y., Wen, J., Wu, H., Zhao, Z., Chen, L., & Ning, J. (2026a). *Hsr radiation pat-*
655 *terns and virtual shot gathers – data [dataset].* Zenodo. doi: 10.5281/zenodo
656 .19944304

657 Shi, Y., Wen, J., Wu, H., Zhao, Z., Chen, L., & Ning, J. (2026b). *Hsr radiation pat-*
658 *terns and virtual shot gathers – software [software].* Zenodo. doi: 10.5281/
659 zenodo.19944288

660 Wang, H., & Chen, J. (2025). Frequency-domain elastic-wave full-waveform in-
661 version based on the synthetic data from high-speed train. *Chinese Journal of*
662 *Geophysics (in Chinese)*, *68*(4), 1430–1443. doi: 10.6038/cjg2024R0515

663 Wang, L., Ren, Z., & Bao, Q. (2025). Full-waveform inversion of rayleigh
664 wave from high-speed-train seismic data for shallow-surface velocity build-
665 ing. *Chinese Journal of Geophysics (in Chinese)*, *68*(4), 1444–1456. doi:
666 10.6038/cjg2024S0160

667 Wang, X., Chen, W., Wen, J., Ning, J., & Li, J. (2019). The applications of syn-
668 chrosqueezing time-frequency analysis in high-speed train induced seismic data
669 processing. *Chinese Journal of Geophysics(in Chinese)*, *62*(6), 2328–2335. doi:
670 10.6038/cjg2019M0658

671 Wen, J., Bao, T., Feng, Y., & Ning, J. (2019). Pku rose array: A road seismologi-
672 cal array deployed by peking university. *Acta Scientiarum Naturalium Univer-*
673 *sitatis Pekinensis(in Chinese)*, *55*(5). doi: 10.13209/j.0479-8023.2019.078

674 Wen, J., Shi, Y., & Ning, J. (2021). Measurement of high-speed rail surface-wave
675 phase-velocity dispersion. *Chinese Journal of Geophysics(in Chinese)*, *64*(9),
676 3246–3256. doi: 10.6038/cjg2021P0252

677 Xiao, Y., Wen, J., Yu, D., & Wen, X. (2013). Flexural wave propagation in beams
678 with periodically attached vibration absorbers: Band-gap behavior and band
679 formation mechanisms. *Journal of Sound and Vibration*, *332*(4), 867–893. doi:
680 10.1016/j.jsv.2012.09.035

681 Yang, Y.-B., Wu, Y.-S., & Chang, D. (2003). Train-induced wave propagation in
682 layered soils using finite/infinite element simulation. *Soil Dynamics and Earth-*
683 *quake Engineering*, *23*(4), 263–278. doi: 10.1016/S0267-7261(03)00003-4

Yang, Y.-B., Yau, J.-D., & Hsu, L.-C. (1997). Vibration of simple beams due to trains moving at high speeds. *Engineering Structures*, *19*(11), 936–944. doi: 10.1016/S0141-0296(97)00001-1

Yin, C., Shi, Y., Wu, H., Wen, J., & Ning, J. (2024). Theoretical analysis of generating virtual seismic gatherings through high-speed rail-induced subsurface seismic wave fields. *Chinese Journal of Geophysics(in Chinese)*, *67*(1), 251–260. doi: 10.6038/cjg2023P0377

Zhang, H., Wang, B., Ning, J., & Li, Y. (2019). Interferometry imaging using high-speed-train induced seismic waves. *Chinese Journal of Geophysics (in Chinese)*, *62*(6), 2321–2327. doi: 10.6038/cjg2019M0676